APL Materials

RESEARCH ARTICLE | MARCH 02 2026

Preparation and evaluation of alexandrite, forsterite, and topaz substrates for the epitaxial growth of rutile oxides

Monique Kubovsky ; Yorick A. Birkhölzer ; Luka B. Mitrovic ; Hanjong Paik ; George R. Rossman ; Darrell G. Schlom

APL Mater. 14, 031103 (2026)
https://doi.org/10.1063/5.0312234

AIP Publishing

Preparation and evaluation of alexandrite, forsterite, and topaz substrates for the epitaxial growth of rutile oxides

Cite as: APL Mater. 14, 031103 (2026); doi: 10.1063/5.0312234
Submitted: 14 November 2025 • Accepted: 12 February 2026 •
Published Online: 2 March 2026

Monique Kubovsky,[1] Yorick A. Birkhölzer,[2,a)] Luka B. Mitrovic,[2] Hanjong Paik,[1,2,b)] George R. Rossman,[3,c)] and Darrell G. Schlom[1,2,4,5,d)]

AFFILIATIONS

[1] Platform for the Accelerated Realization, Analysis, and Discovery of Interface Materials (PARADIM), Cornell University, Ithaca, New York 14853, USA
[2] Department of Materials Science and Engineering, Cornell University, Ithaca, New York 14853, USA
[3] Division of Geology and Planetary Science, California Institute of Technology, Pasadena, Califronia 91125, USA
[4] Kavli Institute at Cornell for Nanoscale Science, Ithaca, New York 14853, USA
[5] Leibniz-Institut für Kristallzüchtung, Max-Born-Str. 2, 12489 Berlin, Germany

[a)] **Author to whom correspondence should be addressed:** y.birkholzer@cornell.edu
[b)] **Present address:** School of Electrical and Computer Engineering, The University of Oklahoma, Norman, Oklahoma 73019, USA.
[c)] Deceased.
[d)] **URL:** https://schlom.mse.cornell.edu

ABSTRACT

Metal–insulator transitions and superconductivity in rutile-structured oxides hold promise for advanced electronic applications, yet their thin film synthesis is severely hindered by limited substrate options. Here, we present three single-crystalline substrates, $BeAl_2O_4$, Mg_2SiO_4, and $Al_2SiO_4(F,OH)_2$, prepared via optimized thermal and chemical treatments to achieve atomically smooth surfaces suitable for epitaxial growth. Atomic force microscopy confirms atomic step-and-terrace surface morphologies, and oxide molecular-beam epitaxy growth on these substrates demonstrates successful heteroepitaxy of rutile TiO_2, VO_2, NbO_2, and RuO_2 films. Among these unconventional substrates, $BeAl_2O_4$ exhibits exceptional thermal and chemical stability, making it a versatile substrate candidate. These findings introduce new substrate platforms that facilitate strain engineering and exploration of rutile oxide thin films, potentially advancing the study of their strain-dependent physical properties.

I. INTRODUCTION

Experimental evidence for strain-induced superconductivity was found in epitaxial thin films of RuO_2 under large compressive strain.[1,2] This is a very remarkable result, since it was the first report of the induction of superconductivity in any material that does not superconduct in its bulk form but does become a superconductor in thin film form by the application of epitaxial strain. This motivates us to expand the toolbox for strain engineering of more oxides with the rutile structure. Conflicting reports regarding a possible altermagnetic ground state in RuO_2 have further fueled interest in the synthesis of rutile oxides.[3–8] In addition to the possibility of discovering superconductivity in rutile oxide thin films, rutiles are a target of research due to their metal–insulator transitions, such as those in VO_2 and NbO_2,[9–11] as well as possible altermagnetism in ReO_2.[12] Transition metal rutile oxides are also interesting due to their catalytic properties,[13] as well as the high spin-polarization of CrO_2.[14,15] A comprehensive overview of rutiles and birutiles has been published by Hiroi.[16]

Historically, much work in the oxide thin film community has focused on perovskites with the generalized chemical formula ABO_3. Among the commercially available oxide single crystal substrates for

thin film growth, the vast majority are perovskites or layered perovskites with the Ruddlesden–Popper structure with the generalized formula A_2BO_4.[17] Rutiles as well as the B-site of ABO_3 perovskites consist of exclusively octahedrally coordinated metal cations. A key difference between the perovskite and rutile structures is that in the former, all octahedra are corner-sharing, whereas the hallmark of the rutile structure is an edge-sharing chain of octahedra along the rutile *c* axis. This gives rutile properties with strong anisotropy. A well-known example is the strong birefringence in TiO_2.

The only two commercially available substrates with the rutile crystal structure are TiO_2 and MgF_2. In a research environment where sample synthesis is not limited by the thermal budget of back-end-of-line-compatible processes, there is a trend to explore the higher synthesis temperatures to improve structural perfection. This regime often enables adsorption controlled growth, which typically unlocks the best thin film properties.[18] This approach recently took a massive step forward through the availability of powerful CO_2 substrate laser heaters that can directly heat oxide substrates.[19,20] Regarding high-temperature stability, TiO_2 is not an ideal substrate, as it rapidly reduces at elevated temperatures and low oxygen partial pressures, which are needed to stabilize intermediate-valence oxides, such as TaO_2. Even more dramatically, we found that MgF_2 already decomposes around 550 °C. An additional challenge to the growth of an oxide (e.g., TiO_2) on MgF_2 is the propensity of the substrate to be oxidized to form a volatile fluoride gas (e.g., TiF_4) through the following reaction:

$$2\ MgF_2 + Ti + O_2 \rightarrow 2\ MgO + TiF_4. \quad (1)$$

At 800 K, this reaction is favorable with ΔG^0 of −257.8 kJ mol^{-1} of MgF_2.[21] To epitaxially strain rutile thin films, more substrates with a rutile-like structure are, thus, needed.

The literature on the bulk single crystal growth of rutile substrates is sparse. Two different rutiles, one with small (GeO_2) and one with large (SnO_2) lattice parameters, stand out in particular. In the quest for ultrawide-bandgap semiconductors, Chae *et al.*[22] demonstrated flux-grown GeO_2 as a rutile substrate, albeit with rather small sample sizes up to 4 × 2 mm^2. Recently, Galazka *et al.*[23] demonstrated top-seeded solution growth of rutile GeO_2 with diameters up to 15 mm from which he was able to successfully prepare substrates with dimensions of 5 × 5 mm^2. While GeO_2 promises to be a good substrate for MnO_2 and CrO_2 with similarly small lattice parameters; here, we are looking for new substrates with a larger lattice parameter. On that note, it is worth mentioning that Galazka *et al.* published the growth of rutile SnO_2 by physical vapor transport (PVT) with diameters up to 25 mm and cut substrates with dimensions of 5 × 5 mm^2.[24] Despite the promising lattice mismatch of SnO_2 to larger rutiles, it is not stable at high temperatures.[25] This makes it not suitable for the growth of materials such as TaO_2, which require temperatures around 1000 °C for crystallization.

The ideal substrate for epitaxy is stable under both oxidizing and reducing conditions at elevated temperatures. This criterion motivated our search beyond the ubiquitous transition-metal oxides with multiple valence states. While isostructural substrates would be ideal for the synthesis of rutile thin films, non-rutile substrates can, in principle, be used for heteroepitaxy. An early such example is the epitaxial synthesis of TiO_2 on Al_2O_3 by Fukushima *et al.*[26] They used the concept of the near-coincidence-site lattice (NCLS)[27] to explain the orientational relationships between the film and Al_2O_3 substrate.

While our group and others have confirmed that single-crystalline heteroepitaxy of (101)-oriented rutile-structured oxide thin films is possible on Al_2O_3 $(1\bar{1}02)$ (*r*-plane sapphire), the resulting layers are highly anisotropically strained at best. While one in-plane direction matches commensurately [as for example in the case of TaO_2 on Al_2O_3 $(1\bar{1}02)$], the orthogonal in-plane direction suffers from a very large (≈10%) mismatch.

To expand the playing field for rutile epitaxy, in this article, we present three materials that can serve as substrates for rutile heteroepitaxy: $BeAl_2O_4$, Mg_2SiO_4, and $Al_2SiO_4(F,OH)_2$. In Table I, the lattice parameters of these orthorhombic materials are summarized. In Fig. 1, the rutile structure is depicted alongside topaz, forsterite, and alexandrite to highlight the similar structural motif shared by all structures: chains of edge-sharing oxygen octahedra along the *c* axes.

A prerequisite for optimal epitaxial thin film growth is a high-quality crystalline substrate with an atomically flat surface with controlled surface termination.[32] We, therefore, present thermal and chemical treatments to prepare such surfaces.

TABLE I. Lattice parameters of rutile, forsterite, alexandrite, and topaz.

Compound	*a* (Å)	*b* (Å)	*c* (Å)	References
TiO_2	4.594	4.594	2.959	28
Mg_2SiO_4	4.753	10.199	5.981	29
$BeAl_2O_4$	4.429	9.407	5.478	30
$Al_2SiO_4(F,OH)_2$	4.667	8.834	8.395	31

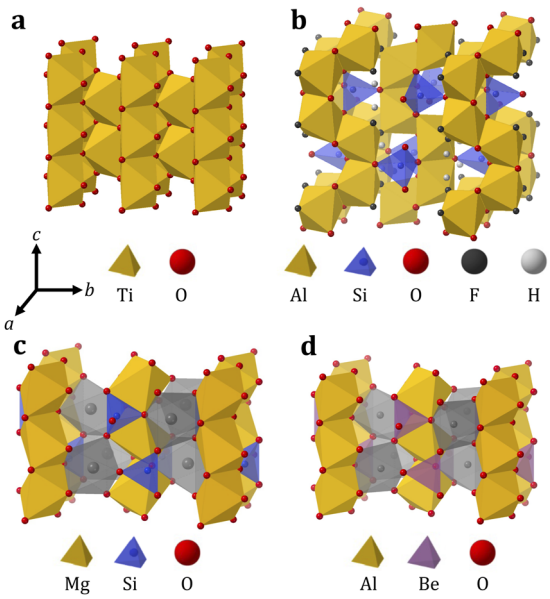

FIG. 1. Schematics of the (a) rutile, (b) topaz, (c) forsterite, and (d) alexandrite crystal structures. The edge-sharing oxygen octahedra forming the common motif along the *c* axis are highlighted in yellow. The octahedral Mg- and Al-sites outside the chains are shown in gray [(c) and (d)].

TABLE II. Expected out-of-plane orientation of film and substrate pairs.

Substrate	Film
Alexandrite or forsterite (010)	Rutile (101) or (010)
Alexandrite or forsterite (001)	Rutile (001)
Topaz (010)	Rutile (010)
Topaz (001)	Rutile (001)

$BeAl_2O_4$ is known under the mineral names chrysoberyl and alexandrite (when Cr-doped). We purchased the substrates from Northrop Grumman Synoptics, a US-based manufacturer of laser crystals. The 0.08 wt. % Cr-doped $BeAl_2O_4$ was grown by the Czochralski method. The Czochralski growth of $BeAl_2O_4$ dates back to the 1960s,[33] and commercial alexandrite lasers (λ = 755 nm) are well-established for applications such as hair and tattoo removal since the 1990s.[34,35] In contrast to the next two materials we introduce in this article, there are no reports of using $BeAl_2O_4$ as a substrate for epitaxial growth. The high structural quality of these crystals is reflected in a narrow rocking curve full width at half maximum (FWHM) of 15 arcsec.

Mg_2SiO_4 is known under its mineral name forsterite. We purchased the Czochralski-grown raw material from Oxide Corp, Japan, and had it diced and polished by the German company SurfaceNet. The Czochralski growth of Mg_2SiO_4 was described in the early 1970s.[36,37] In this work, we refer to forsterite and isostructural alexandrite using the non-standard (but most commonly used) *Pbnm* setting of space group No. 62, which leads to matching Miller indices for several orientations of rutile adlayers as well as the substrate.[38]

The fluoride-dominant topaz mineral used in this study was of Brazilian origin and oriented and polished by the German vendor Crystec. The reliance on a natural mineral stems from the impossibility of growing topaz from the melt and the insufficient size of early hydrothermally grown crystals,[39] which were at least two orders of magnitude too small for substrate applications.

A significant recent advance was reported by Setkova *et al.*,[40] who not only synthesized mm-scale synthetic topaz but also achieved a controlled expansion of the lattice parameter by up to 3% through the partial substitution of Al with Ga and Si with Ge. Crucially, however, these crystals were grown on natural topaz seeds, and their resulting size and quality were insufficient to meet the demands posed on substrates for epitaxy.

All substrates used in this study were available in dimensions up to 10 × 10 × 1 mm^3. The expected orientations of the films for various substrate orientations are summarized in Table II and will be discussed in detail in Sec. II.

II. ORIENTATIONAL MATCH OF ALEXANDRITE, FORSTERITE, AND TOPAZ SUBSTRATES WITH RUTILE

In this article, we present multiple orientations of three different substrates for rutile epitaxy, leading to multiple possible epitaxial interfaces. Our choice of substrates is guided by three factors: (1) the availability of single crystals with excellent structural quality and of sufficient size to yield 10 × 10 mm^2 substrates, (2) a similar structural motif to a rutile so that what we call "local epitaxy" can occur during growth, and (3) an NCSL with a high concentration of NCSL sites at the interface between substrate and film and small lattice mismatch. By local epitaxy, we refer to sub-unit cell structural elements that are similar in the film and substrate and allow depositing atoms to continue the structural motif between substrate and film via epitaxy. We particularly focus on continuity in the type and arrangement of coordination polyhedra. This can be viewed as following Pauling's rules[41] across interfaces.[42] The specific substrates and orientations were deliberately selected for the growth of rutile films by carefully considering their crystal structures, and as we report, all were found to provide epitaxial growth for rutile films. A striking feature of the rutile structure is the chains of edge sharing TiO_6 octahedra it contains. It is this structural motif that was the focus of our local epitaxy approach. In selecting potential substrates, we selected oxide (or oxyfluoride) substrates with this same structural element. The similarity in structures is evident in Fig. 1, where the edge-sharing chains of octahedra are colored yellow in rutile and the three substrates selected for this study. Inspired by the NCLS model,[27] we designed heterostructures wherein the oxygen octahedral network across the interface between substrate and film is preserved as best as possible. In Secs. II A–II C, we compare the effective in-plane lattice parameters of bulk-like, unstrained film and substrate pairings and schematically sketch the expected cross-sectional interfaces.[43]

A. Substrates for (001) rutile thin films

Let us start with (001)-oriented films, where for an undistorted rutile crystal structure, the in-plane directions are the indistinguishable *a* and *b* axes, respectively. Figure 2 compares a selection of rutile oxide lattice parameters[16] with $BeAl_2O_4$ (001) and topaz (001). For simplicity, we ignore the fact that some rutile-like oxides, such as MoO_2 and NbO_2, have polymorphs with slightly distorted crystal structures with lower symmetry than the idealized rutile. In this article, we discuss pseudotetragonal $a = b$ for all rutile-like oxides.

In Fig. 3, we show the interface between rutile TiO_2 (001) and $BeAl_2O_4$ (001) as well as between rutile VO_2 (001) and topaz (001) in a cross-sectional schematic. Additional perspectives along the ⟨110⟩

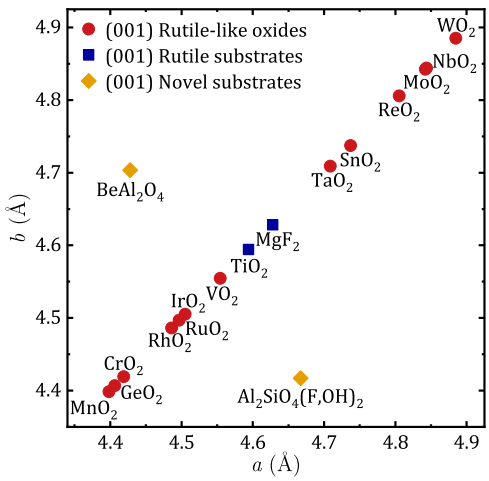

FIG. 2. In-plane lattice parameters of select (001)-oriented rutile-like oxides, commercially available rutile substrates, alexandrite, and topaz.

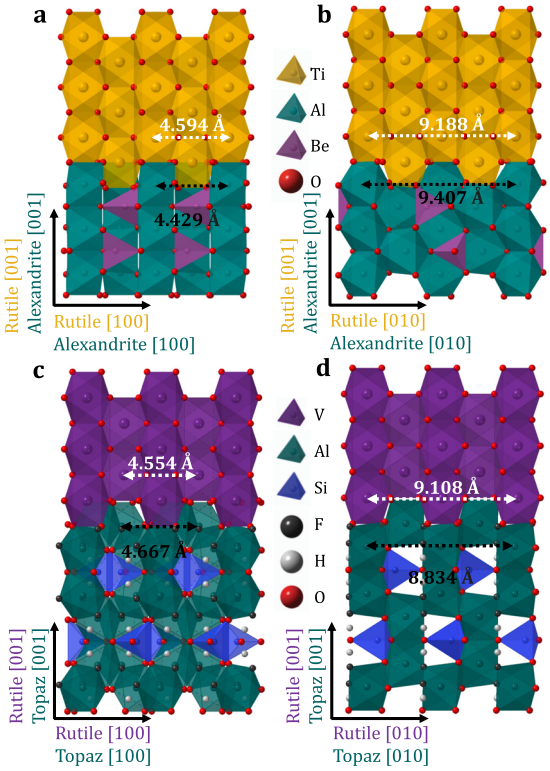

FIG. 3. Cross-sectional schematic of TiO_2 (001) on $BeAl_2O_4$ (001) viewed along the substrate [100] (a) and [010] directions (b); VO_2 (001) on $Al_2SiO_4(F,OH)_2$ (001) viewed along the substrate [001] (c) and [010] direction (d).

directions are illustrated in Fig. 14. The geometric match between the substrate and thin film at the interface suggests that high quality epitaxial rutile thin films can be grown on $BeAl_2O_4$ (001). An example is shown later in this article. Being able to template (001) rutile growth is particularly exciting since this plane has a very high surface energy compared to the (010) and (101) orientations, which are discussed in the following subsections.[44]

B. Substrates for (010) rutile thin films

In the case of (010)-oriented rutile growth, the in-plane lattice parameters are the *a* and *c* axes. Figure 4 compares select rutile lattice parameters[16] with $BeAl_2O_4$ (010), Mg_2SiO_4 (010), and topaz (010). In Fig. 5, we schematically show the interface between RuO_2 (010) and Mg_2SiO_4 (010), as well as RuO_2 (010) and topaz (010).

Preliminary attempts to grow RuO_2 on Mg_2SiO_4 (010) led to (010)-oriented rutile growth despite the large lattice mismatch. This result is particularly interesting because the rutile *c* axis lies in-plane in this geometry and can potentially be subject to a large compressive strain.

C. Substrates for (101) rutile thin films

Finally, we examine the case of (101)-oriented rutile growth. For such films, the in-plane directions are $[10\bar{1}]$ and [010] with

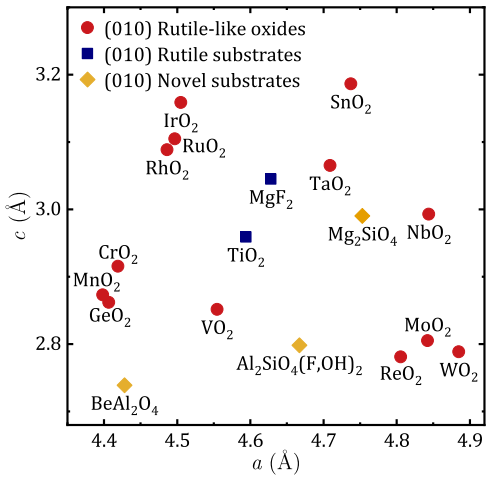

FIG. 4. In-plane lattice parameters of rutile (010) materials compared with commercially available rutile substrates, alexandrite, forsterite, and topaz.

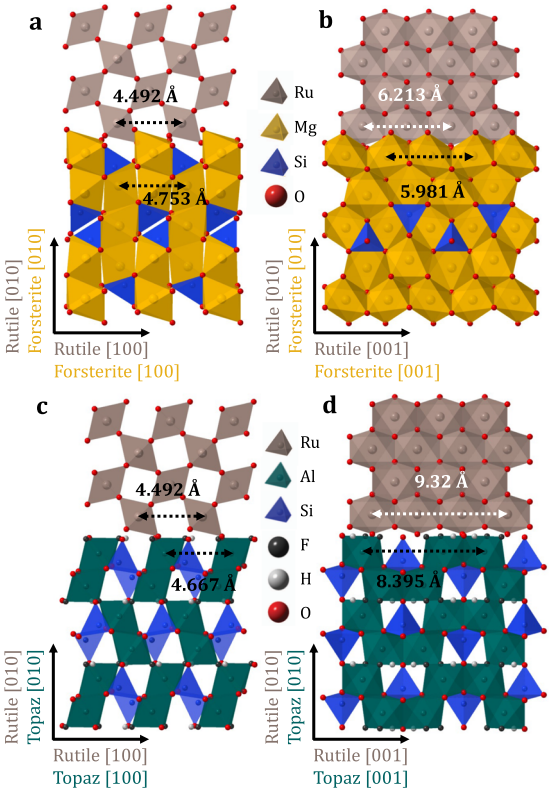

FIG. 5. Cross-sectional schematic of RuO_2 (010) on Mg_2SiO_4 (010) [(a), (b)] and RuO_2 (001) on $Al_2SiO_4(F,OH)_2$ (001) viewed along the substrate [001] (a) and [100] directions [(c), (d)].

effective lengths $\sqrt{a^2+c^2}$ and b, respectively. Figure 6 summarizes the resulting in-plane parameters of select rutile oxides[16] and compares them with $BeAl_2O_4$ and Mg_2SiO_4 (010) as well as Al_2O_3 $(1\bar{1}02)$.

Figure 7 shows the expected interface between Mg_2SiO_4 (010) and NbO_2 (101), which we experimentally verified; see Sec. III D. The same orientational relationship was also experimentally verified for RuO_2 (101) on $BeAl_2O_4$ (010) (not shown). We note that the forsterite (010) substrates can, thus, template both rutile (010) and rutile (101) epitaxial growth depending on the lattice mismatch.

Having outlined the expected orientational relationships based on bulk lattice parameters and in schematic form, in Sec. III, we present experimental annealing results of the aforementioned substrates, showing that they can be prepared with an atomically smooth step-and-terrace surface morphology as is desired for epitaxial overgrowth. The development of substrate termination recipes that provide smooth step-and-terrace surfaces with known termination has been a major boon to the growth of oxide films on perovskite,[19,32,45–54] rock salt,[19] rutile,[55] sapphire,[56–58] and cubic zirconia[59,60] substrates. Our work extends this ability to rutile-related substrates.

We use atomic force microscopy to image the surface of the substrates before and after thermo-chemical treatment. Our preferred treatment is an *in situ* thermal annealing step inside the growth chamber, which was performed at a background pressure of distilled ozone of 1×10^{-6} Torr to prevent unintentional substrate reduction at elevated temperatures. See the section titled "Methods" for further details. The Sec. III summarizes the best results for each substrate. A comprehensive dataset comparing *in situ* laser-annealed substrates with *ex situ* furnace-annealed samples is available in the Appendix, recognizing that mid-infrared laser substrate heating systems are not yet widely adopted.

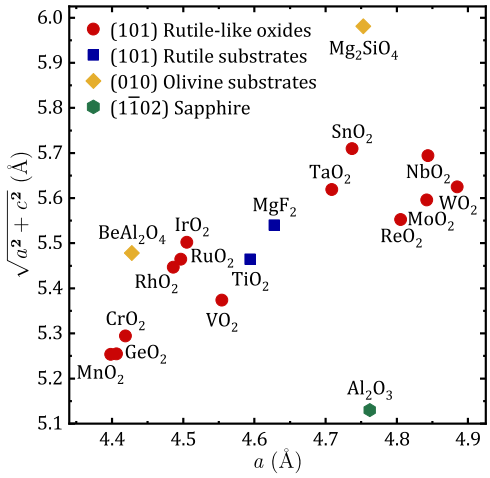

FIG. 6. In-plane lattice parameters of select (101)-oriented rutile-like oxides, commercially available rutile and sapphire substrates, alexandrite, and forsterite. Note that for undistorted rutile, $a = b$.

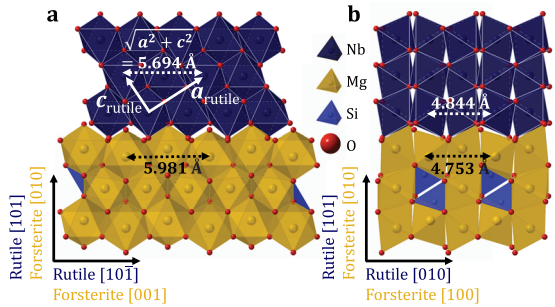

FIG. 7. Cross-sectional schematic of rutile NbO_2 (101) on Mg_2SiO_4 (010) projected along [100] (a) and [001] (b).

III. RESULTS

A. $BeAl_2O_4$

Beginning with the (001) orientation of $BeAl_2O_4$, the as-received substrate in Fig. 8(a) presents a step-and-terrace surface, where the terraces are of uniform width but have meandering step edges. Out of the set of preparation procedures we used, the best

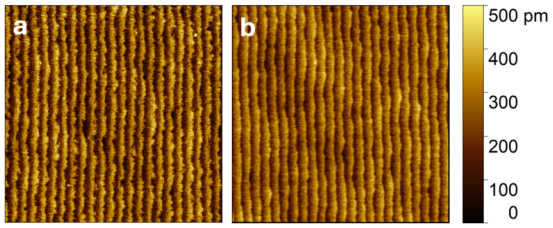

FIG. 8. 2 × 2 μm AFM scans of (001) $BeAl_2O_4$ (a) in the as-received state and (b) after laser annealing at 1250 °C for 200 s.

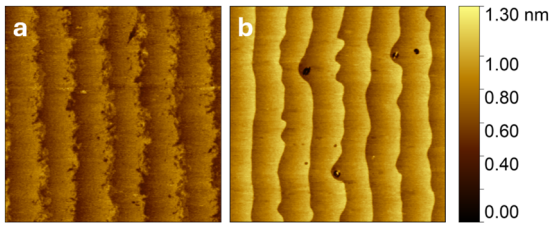

FIG. 9. 2 × 2 μm AFM scans of (010) $BeAl_2O_4$ (a) in the as-received state and (b) after furnace annealing at 900 °C for 1 h.

results were produced by laser annealing at 1250 °C for 200 s, shown in Fig. 8(b). Higher annealing temperatures (Fig. 15) caused holes to form within the terraces, as well as excessive step meandering. In addition, the procedure reduced the rms roughness from less than 0.2 nm to less than 0.1 nm. Annealing produced steps ~0.25 nm high, which corresponds to 1/2 of the unit cell height in the [001] direction. Figure 16 presents a possible model describing this behavior.

The as-received (010) $BeAl_2O_4$ surface is similarly rough to the (001) surface. Laser annealing for 200 s revealed that this plane becomes doubly terminated, signified by triangular holes that change orientations on alternating terraces (Fig. 17). As the desired step-and-terrace surface morphology was not achieved through rapid *in situ* laser annealing, we used a tube furnace (Fig. 18) to explore lower temperatures and longer annealing times.[61] By furnace annealing at 900 °C for an hour in 1 atm oxygen pressure, we achieved very smooth, uniform terraces and straightened steps with minimal meandering (Fig. 9). The rms roughness of both the as-received and annealed states was below 0.2 nm. Annealing at higher temperatures causes raised needle structures with surrounding pits to form. Step height measurements reveal that the (010) $BeAl_2O_4$ surface becomes doubly terminated through the formation of steps of fractional unit-cell height. Some samples had step heights between 0.35 and 0.4 nm, while others had heights around 0.55 nm. These values roughly correspond to 2/5 and 3/5 of the unit cell height. While the exact surface termination is currently unknown, we present two possible models describing this behavior in Fig. 19. To reduce inhomogeneity and the tendency of some films to form twins, a single-terminated surface would be more desirable. Future work could explore the influence of vicinal miscut angle and more finely tuned annealing conditions to achieve additional control of the step height.

B. Mg_2SiO_4

Figure 10 shows AFM scans before and after laser annealing at 1300 °C for 200 s. This procedure adequately smoothed out the steps, maintained terrace width uniformity, and produced minimally waved, parallel steps. The rms roughness remained ≈0.3 nm as a result of the annealing. The prepared samples had step heights around 1 nm, which is in very good agreement with the expected height of a single-unit-cell step. The results from additional annealing procedures at other temperatures are shown in Fig. 20. Due to the limited availability of high-quality raw material, other orientations of Mg_2SiO_4 have not been explored thus far.

C. $Al_2SiO_4(F,OH)_2$

Unlike the laboratory-grown substrates presented in Secs. II A and II B, the topaz used in this study was of natural origin. While the artificial growth of topaz has been attempted via the hydrothermal method, the dimensions of the crystals reported in the literature thus far remain too small for thin film studies.[39] Another challenge is the lack of compositional control regarding the F/OH ratio in natural or lab-grown topaz. We expect that the high fugacity of F- and OH-containing species, e.g., HF and H_2O, poses a serious limitation on the accessible temperature range for thin film growth.

Here, we use substrates of 1 mm thickness and 3 × 5, 5 × 5, and 10 × 10 mm^2 lateral dimensions. Both orientations of topaz were etched in a buffered HF solution for 60 s prior to any attempted annealing. Even without thermal annealing, this step alone already drastically improves the surface quality of topaz.[62]

For the (001) surface, laser annealing at 700 and 800 °C for 200 s resulted in changes in surface morphology but with little change in rms roughness compared with the as-received substrate (Fig. 21). At high temperatures, the RHEED patterns began to fade, suggesting that the fluorine may be leaving the surface. Laser annealing at lower temperatures before the RHEED patterns deteriorate fails to substantially change the surface beyond its as-received state. To further investigate the lower anneal temperatures, we used a tube furnace. Furnace annealing at 750 °C for an hour successfully produced much smoother steps than the as-received samples (Figs. 11 and 22). The rms roughness of both the as-received and annealed states was below 0.2 nm. The annealed substrates had step heights around 0.8 nm, which matches the unit cell height of (001) topaz.

Acid etching the (010) topaz defined the step-and-terrace structure and left the steps much smoother than the as-received state. Unfortunately, the laser annealed samples had rough, meandering steps (Fig. 23). Similar issues with the RHEED patterns were observed for the (010) surface as for the (001) orientation. Annealing

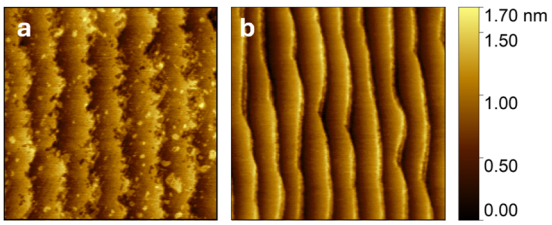

FIG. 10. 2 × 2 μm AFM scans of (010) Mg_2SiO_4 (a) in the as-received state and (b) after laser annealing at 1300 °C for 200 s.

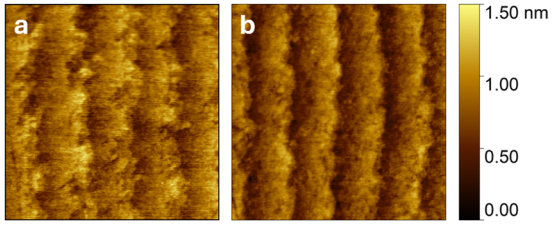

FIG. 11. 2 × 2 μm AFM scans of (001) $Al_2SiO_4(F,OH)_2$ (a) in the as-received state and (b) after furnace annealing at 750 °C for 1 h.

in a tube furnace at 1 atm oxygen background at lower temperatures with longer hold times allowed the steps to straighten out but caused particles to form across the surface (Figs. 12 and 24). It is possible that these particles could be removed with repeated etching in HF acid. The rms roughness of the annealed state increased to <0.6 nm from <0.2 nm, likely due to the particles that formed across the surface. In addition, this preparation produced steps of 0.45 nm, which corresponds to 1/2 of the unit cell height in the [010] direction. At higher annealing temperatures, the surface is terminated with 0.22 nm high steps, each of which has a height of 1/4 of the unit cell. A model of how this quadruple termination may occur is shown in Fig. 25.

When trying to capture the RHEED images of topaz substrates, we frequently observed image-distorting charging artifacts that could not be mitigated by changing the ozone background pressure or increasing the substrate temperature. We ascribe this to the highly electrically insulating nature of topaz.

Attempts to anneal at even higher temperatures $\gg$800 °C led to the irreversible destruction of the surface and the observation of circular arcs in the RHEED pattern, indicative of polycrystallinity.

Hampar and Zussman[63] comprehensively reviewed the thermal breakdown of topaz, suggesting that breakdown begins above 850 °C in air. The authors also reported easy damage of topaz by focused electron beams.[64] We observed RHEED patterns of topaz to fade above 600 °C, which could be due to a combination of electron-beam induced damage and temperature. Of the substrate materials introduced in this article, topaz has the lowest thermal and chemical stability. Fortunately, many rutile oxides can be grown at low temperatures <400 °C.[1,2,65,66]

D. Thin film growth

Having demonstrated successful annealing protocols to prepare smooth surfaces with well-defined, regular steps, we now show some preliminary thin film growth results on these unconventional substrates. We demonstrate five examples of different film and substrate combinations: VO_2 (001) on topaz (001), TiO_2 on alexandrite (001), RuO_2 (010) on topaz (010), RuO_2 (010) on forsterite (010), and NbO_2 (101) on forsterite (010).

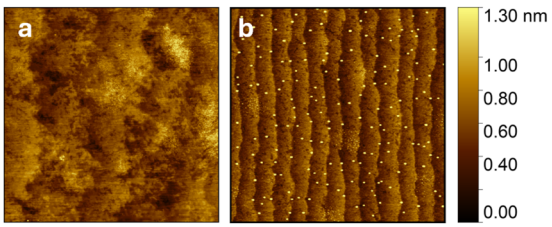

FIG. 12. 5 × 5 μm AFM scans of (010) $Al_2SiO_4(F,OH)_2$ (a) in the as-received state and (b) after furnace annealing at 750 °C for 1 h.

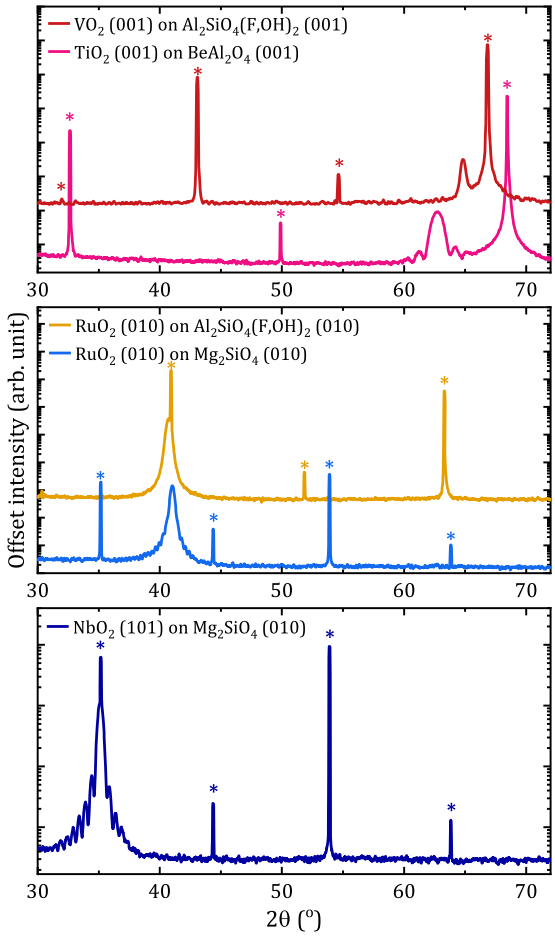

FIG. 13. XRD of epitaxial VO_2, TiO_2, RuO_2, and NbO_2 thin films grown on alexandrite, forsterite, and topaz substrates. The substrate peaks are denoted with asterisks.

The symmetrical $\theta - 2\theta$ XRD scans of these five epitaxial film samples are shown in Fig. 13. For each film, only peaks belonging to a single family of planes were detected, indicating that the films have a single out-of-plane orientation. The in-plane alignment with the substrates and, thus, epitaxial growth was established from the observed RHEED patterns (see Fig. 26) as well as ϕ-scans (see Fig. 27). Furthermore, variable-temperature XRD (see Fig. 28) of the VO_2 film on topaz (001) showed the reversible phase transition between the monoclinic M_1 phase at room temperature and the rutile R phase of VO_2 at high temperature. The detailed study of the microstructure and the physical properties of the differently strained RuO_2 layers will be the topic of a future article.

IV. CONCLUSION

In summary, we have presented three promising single-crystalline substrates that can be thermo-chemically prepared to serve as substrates for epitaxial thin film growth. The ability to produce smooth, regularly stepped substrates provides an ideal starting ground for the exploration of heteroepitaxial thin film growth. The best results thus far have been achieved with Mg_2SiO_4 and $BeAl_2O_4$, whereas achieving a smooth termination of topaz remains an open challenge. In particular, $BeAl_2O_4$ stands out due to its exceptional thermal and chemical stability, increasing its applicability as a substrate for rutiles under a wide variety of optimal growth conditions.

Rutile VO_2, TiO_2, RuO_2, and NbO_2 epitaxial thin films were grown via molecular-beam epitaxy to demonstrate the versatility of topaz $[Al_2SiO_4(F,OH)_2]$, alexandrite ($BeAl_2O_4$), and forsterite (Mg_2SiO_4) substrates. While the case studies examined the growth of rutile, the substrates presented here are also well suited for the growth of other crystalline materials, in particular materials with the alexandrite structure.

V. METHODS

Atomic force microscopy images were recorded *ex situ* in air at room temperature using an Asylum Research Cypher S instrument with NanoWorld Arrow-UHFAuD-10 cantilever probes. Post-processing was performed using Gwyddion (v.2.67).

In situ laser annealing was performed inside a Veeco Gen10 molecular-beam epitaxy chamber equipped with a mid-infrared (10.6 μm) CO_2 laser substrate-heating system built by Epiray. The temperature was controlled using a 7.5 μm wavelength pyrometer probing the backside of the substrate, which was calibrated to the melting point of sapphire. A ramp rate of 200 °C min^{-1} was used up to 1000 °C and 100 °C min^{-1} thereafter. This *in situ* annealing protocol follows the example of Braun *et al.*[19] Distilled ozone was supplied about 41 mm from the center of the front side of the substrate via a water-cooled stainless steel nozzle, and the chamber background pressure was kept at 1×10^{-6} Torr. The base pressure of the chamber is better than 1×10^{-8} Torr.

Rutile RuO_2 thin films were grown by the electron-beam evaporation of ruthenium in an ambient of distilled ozone. NbO_2 thin films were grown using suboxide molecular-beam epitaxy using a Nb_2O_5 charge (H.C. Stark 99.99%) contained in an iridium crucible in a high-temperature MBE effusion cell, as has been used to grow $KNbO_3$ by MBE.[67] The dominant vapor pressure emanating from a Nb_2O_5 charge is tetravalent NbO_2.[25] This suboxide approach avoids the need (and associated flux instability) for the electron-beam evaporation of Nb metal. Suboxide MBE was performed at base pressure without added oxidant. *In situ* RHEED images were collected using a Staib electron gun and kSA camera system at a beam energy of 13 keV.

Furnace annealing was performed in an alumina tube with a flow of 60 ml min^{-1} oxygen gas at atmospheric pressure. Prior to annealing, all substrates were cleaned using isopropanol and dried with nitrogen. In addition, the topaz samples were etched in a buffered HF solution for 60 s.

X-ray diffraction was performed using a PANalytical Empyrean diffractometer, equipped with a hybrid mirror-monochromator and a PIXcel3D detector.

ACKNOWLEDGMENTS

The authors thank Maya Ramesh, Anna S. Park, Tomas A. Kraay, and Steven Button for experimental assistance. This work made use of the thin film facility of the Platform for the Accelerated Realization, Analysis, and Discovery of Interface Materials (PARADIM), which is supported by the NSF under Cooperative Agreement No. DMR-2039380. M.K. acknowledges support through the REU Site: Summer Research Program at PARADIM, which is supported by the NSF under Cooperative Agreement No. DMR-2150446. Y.A.B. acknowledges support from the Dutch Research Council (NWO) through the project *Conductivity on demand—turning an insulator into a metal* with Project No. 019.223EN.017 of the research program RUBICON. L.B.M. was supported as part of the Center for Electrochemical Dynamics and Reactions at Surfaces (CEDARS), an Energy Frontier Research Center funded by the U.S. Department of Energy, Office of Science, Office of Basic Energy Sciences, under Award No. DE-SC0023415. This research was funded, in part, by the Gordon and Betty Moore Foundation's EPiQS Initiative (Grant Nos. GBMF3850 and GBMF9073) to Cornell University.

AUTHOR DECLARATIONS

Conflict of Interest

The author D.G.S. has been granted U.S. Patent No. 11,462,402 (4 October 2022) with the title "Suboxide Molecular-Beam Epitaxy and Related Structures."

Author Contributions

Monique Kubovsky and Yorick A. Birkhölzer contributed equally to this paper.

M.K. performed and analyzed the AFM under the guidance of Y.A.B. Y.A.B. conceived the project and fabricated and analyzed the thin film samples together with L.B.M. and H.P. under the guidance of D.G.S., who suggested these rutile-related substrates. G.R.R. sourced the topaz. M.K. and Y.A.B. wrote the manuscript with input from all authors.

Monique Kubovsky: Data curation (equal); Formal analysis (equal); Investigation (equal); Validation (equal); Visualization (equal); Writing – original draft (equal); Writing – review & editing (equal). **Yorick A. Birkhölzer**: Conceptualization (equal); Data

curation (lead); Formal analysis (lead); Investigation (lead); Methodology (lead); Project administration (equal); Supervision (supporting); Validation (equal); Visualization (equal); Writing – original draft (equal); Writing – review & editing (equal). **Luka B. Mitrovic**: Formal analysis (supporting); Investigation (supporting); Validation (supporting); Writing – original draft (supporting); Writing – review & editing (supporting). **Hanjong Paik**: Data curation (supporting); Formal analysis (supporting); Investigation (supporting). **George R. Rossman**: Investigation (supporting). **Darrell G. Schlom**: Conceptualization (equal); Project administration (equal); Resources (lead); Supervision (lead); Writing – review & editing (equal).

DATA AVAILABILITY

The data that support the findings of this study are available within the article. Additional data related to the growth are available at https://doi.org/10.34863/gp99-em41. Any additional data connected to the study are available from the corresponding author upon reasonable request.

APPENDIX: SUPPORTING STRUCTURAL SCHEMATICS, ATOMIC FORCE MICROSCOPY, REFLECTION HIGH-ENERGY ELECTRON DIFFRACTION, AND X-RAY DIFFRACTION DATA

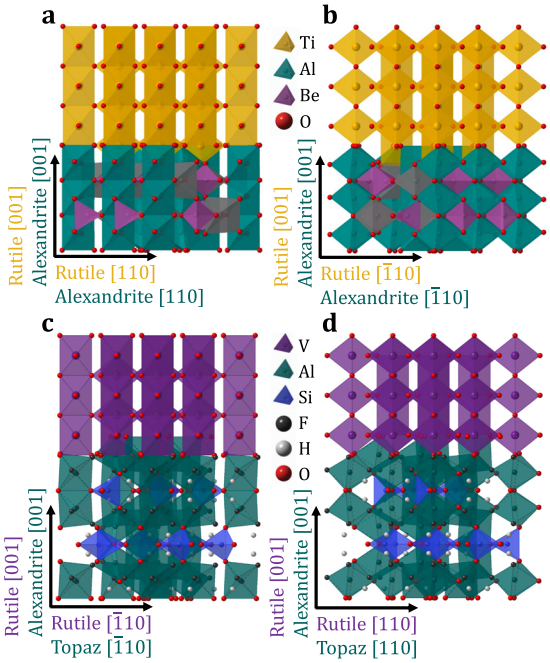

FIG. 14. Cross-sectional schematic of [(a), (b)] TiO_2 (001) on $BeAl_2O_4$ (001) and [(c), (d)] VO_2 on topaz (001). Emphasizing the continuation of the edge-sharing octahedral network along the *c* axis. Complementary views to Fig. 3 rotated 45° around the *c* axis.

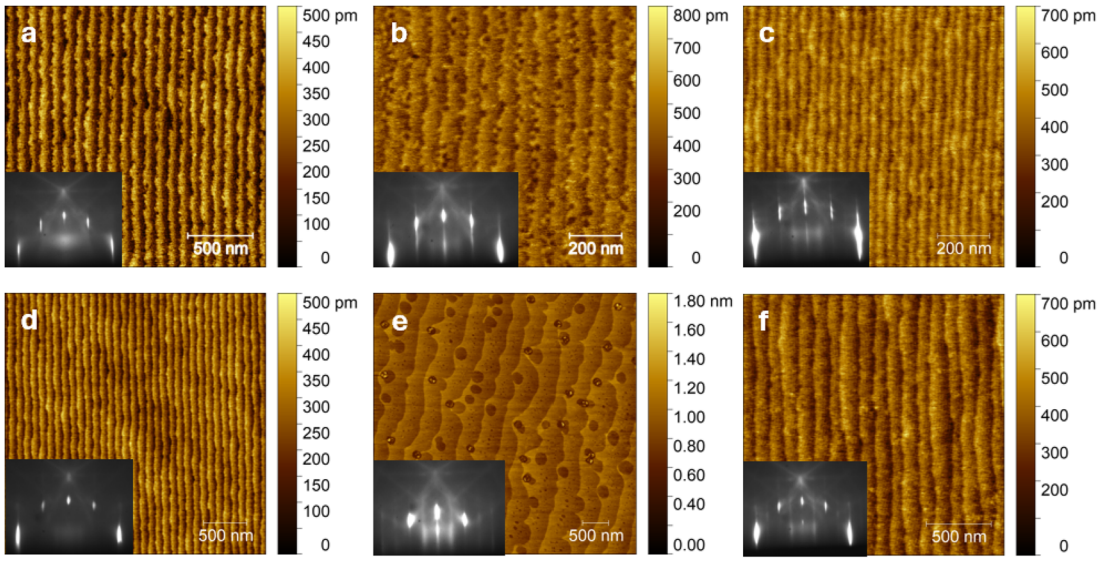

FIG. 15. AFM scans and RHEED patterns of (001) $BeAl_2O_4$ (a) in the as-received state and after (b) laser annealing at 1100 °C for 200 s, (c) 1200 °C for 200 s, (d) 1250 °C for 200 s, (e) 1300 °C for 200 s, and (f) 1400 °C for 200 s.

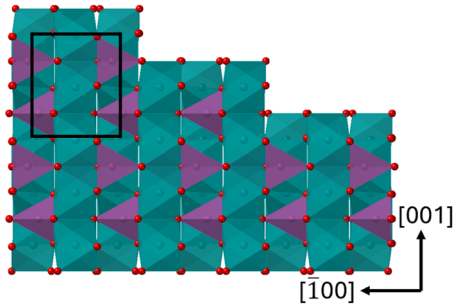

FIG. 16. Cross-sectional schematic of the possible surface termination of a vicinal (001) $BeAl_2O_4$ substrate with 1/2 unit cell step height.

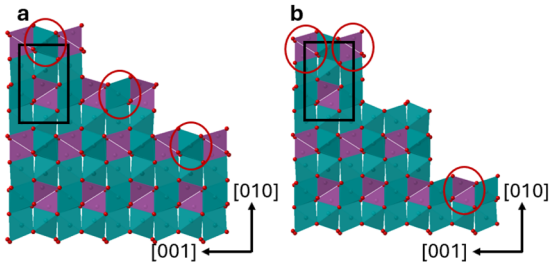

FIG. 19. Cross-sectional schematic of possible surface terminations of vicinal (010) $BeAl_2O_4$ substrates with (a) 2/5 unit cell step height and (b) 3/5 unit cell step height. In (a), the aluminum octahedra face in two different directions on alternating steps, which creates the double termination. In (b), the beryllium dimers only appear in every other step surface, also creating a double termination.

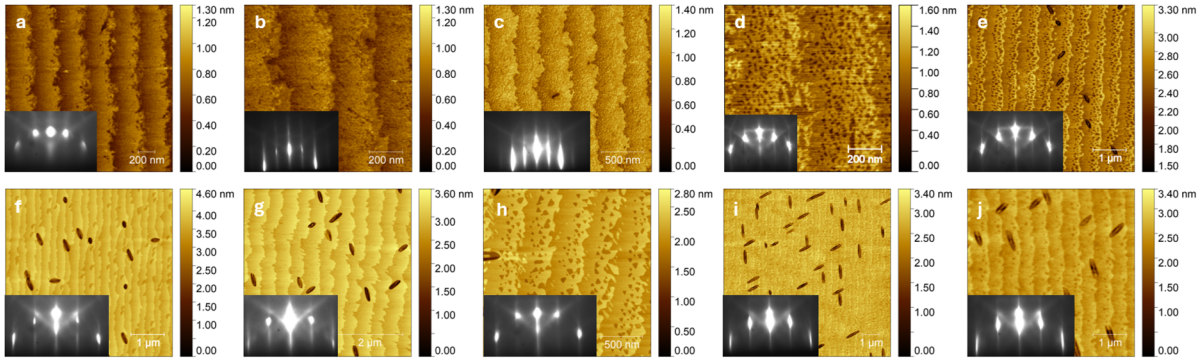

FIG. 17. AFM scans and RHEED patterns of (010) $BeAl_2O_4$ (a) in the as-received state and after (b) laser annealing at 1100 °C for 200 s, (c) 1200 °C for 200 s, (d) 1300 °C for 200 s, (e) 1350 °C for 200 s, (f) 1350 °C for 320 s, (g) 1400 °C for 200 s, (h) 1450 °C for 200 s, (i) 1450 °C for 500 s, and (j) 1500 °C for 200 s.

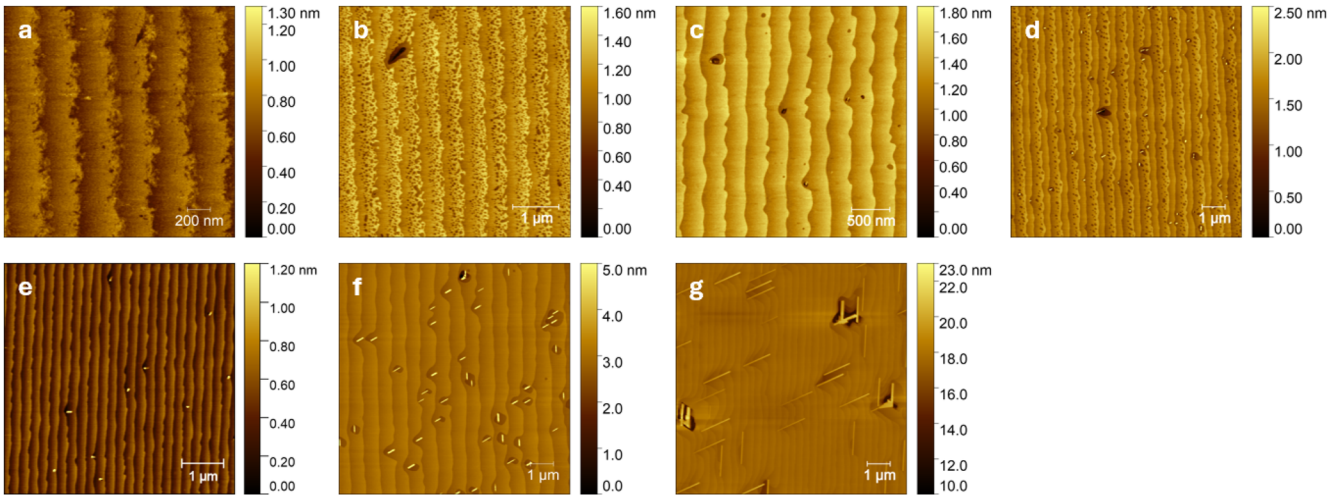

FIG. 18. AFM scans of (010) $BeAl_2O_4$ (a) in the as-received state and after (b) furnace annealing at 850 °C for 2 h, (c) 900 °C for 1 h, (d) 950 °C for 1 h, (e) 1000 °C for 1 h, (f) 1100 °C for 1 h, and (g) 1200 °C for 1 h.

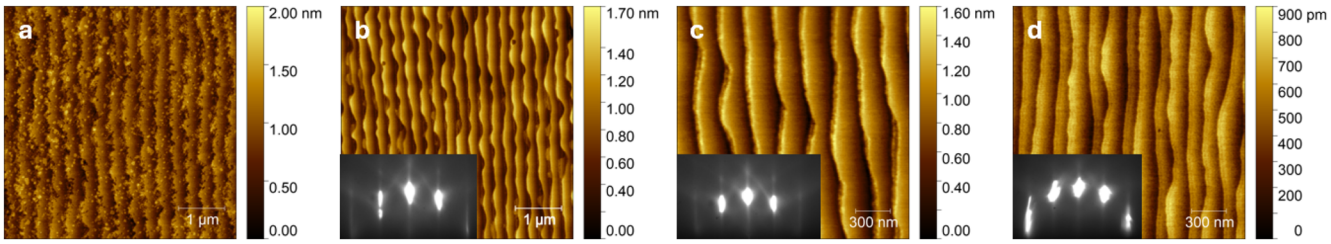

FIG. 20. AFM scans and RHEED patterns of (010) Mg_2SiO_4 (a) in the as-received state and after (b) laser annealing at 1200 °C for 200 s, (c) 1300 °C for 200 s, and (d) 1400 °C for 200 s.

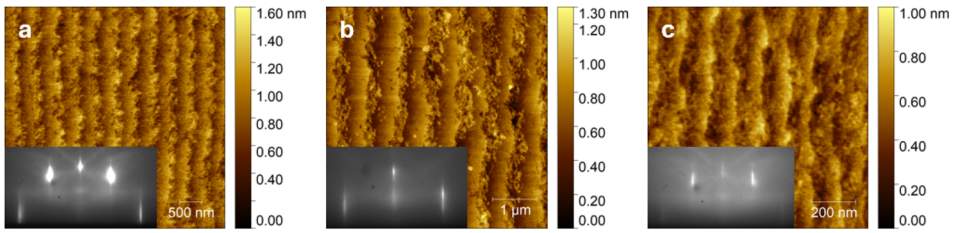

FIG. 21. AFM scans and RHEED patterns of (001) $Al_2SiO_4(F,OH)_2$ (a) after BHF etching followed by (b) laser annealing at 700 °C for 200 s, and (c) 800 °C for 200 s.

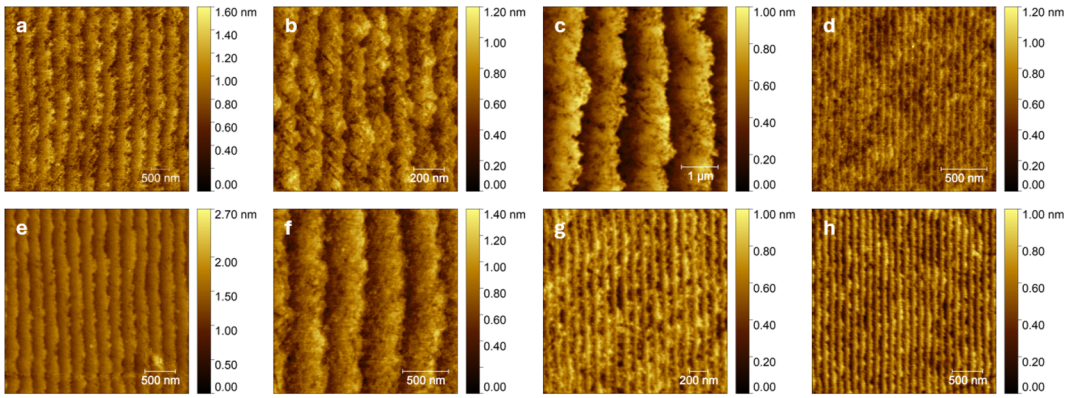

FIG. 22. AFM scans of (001) $Al_2SiO_4(F,OH)_2$ (a) in the as-received state and after (b) furnace annealing at 550 °C for 2 h, (c) 600 °C for 1 h, (d) 650 °C for 1 h, (e) 700 °C for 1 h, (f) 750 °C for 1 h, (g) 800 °C for 1 h, and (h) 850 °C for 1 h.

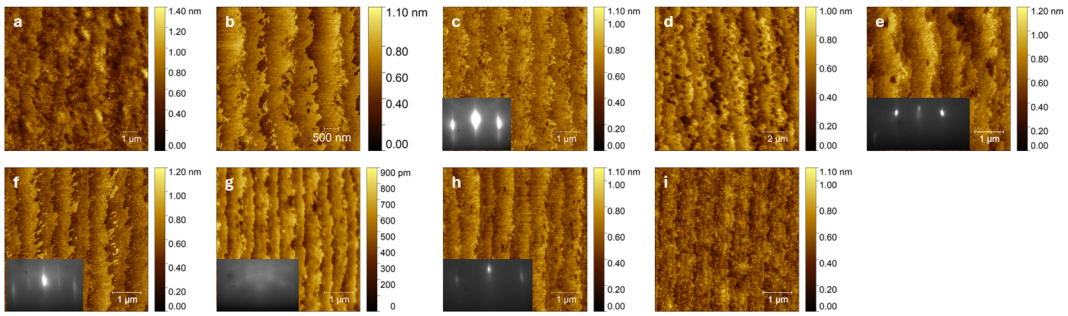

FIG. 23. AFM scans and RHEED patterns of (010) $Al_2SiO_4(F,OH)_2$ (a) in the as-received state and after (b) etching in BHF followed by (c) laser annealing at 700 °C for 200 s, (d) 750 °C for 500 s, (e) 800 °C for 200 s, (f) 850 °C for 200 s, (g) 850 °C for 500 s, (h) 900 °C for 200 s, and (i) 1000 °C for 200 s.

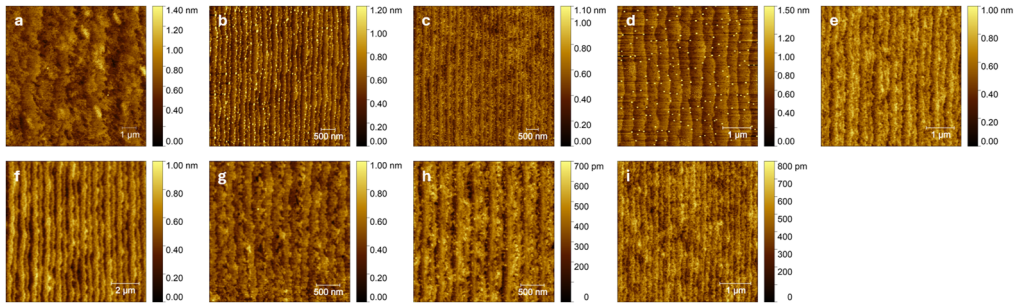

FIG. 24. AFM scans of (010) $Al_2SiO_4(F, OH)_2$ (a) in the as-received state and after (b) furnace annealing at 550 °C for 2 h, (c) 575 °C for 1 h, (d) 600 °C for 1 h, (e) 650 °C for 1 h, (f) 700 °C for 1 h, (g) 750 °C for 1 h, (h) 800 °C for 1 h, and (i) 850 °C for 1 h.

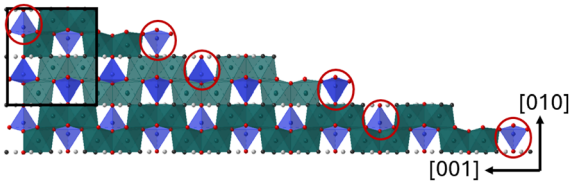

FIG. 25. Cross-sectional schematic of the possible surface termination of a vicinal (010) topaz substrate with quarter-unit-cell steps. The silicon coordination polyhedra face (circled) opposite directions on alternating steps, creating a quadruple termination.

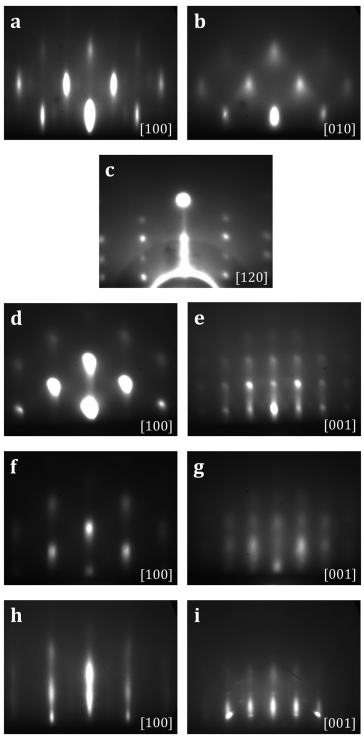

FIG. 26. RHEED patterns recorded at the end of the growth of [(a), (b)] TiO_2 (001) on alexandrite (001), (c) VO_2 (001) on topaz (001), [(d), (e)] RuO_2 (010) on topaz (010), [(f), (g)] RuO_2 (010) on forsterite (010), and [(h), (i)] NbO_2 (101) on forsterite (010). The electron beam was aligned with respect to the substrate Miller indices indicated at the bottom right corner of the panels.

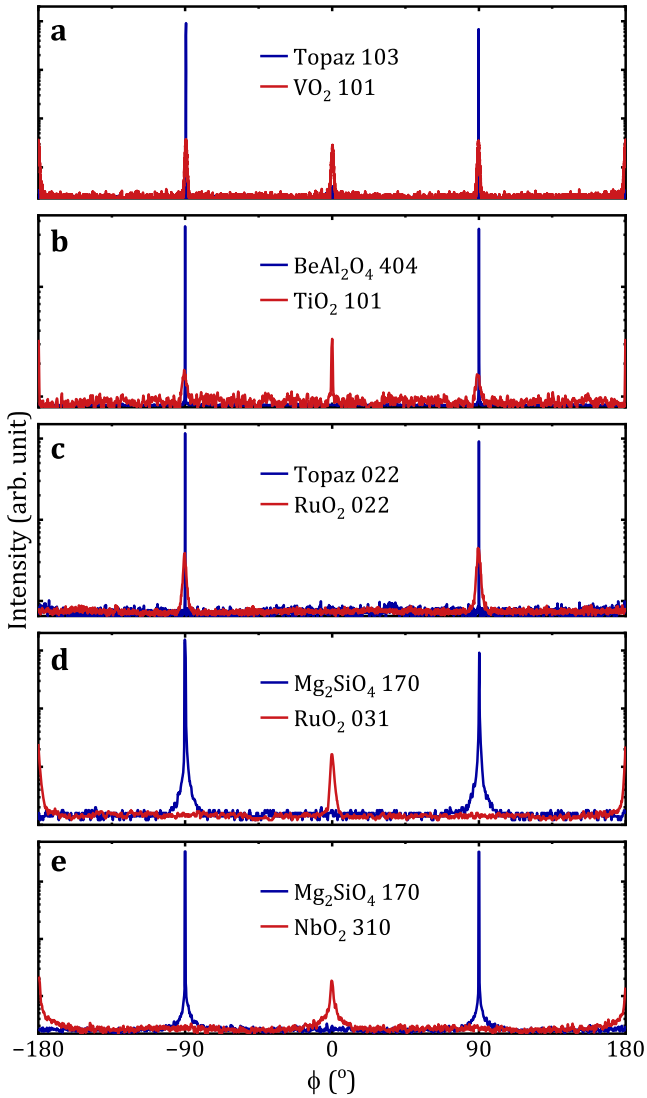

FIG. 27. XRD phi-scans of (a) VO_2 (001) on topaz (001), (b) TiO_2 (001) on alexandrite (001), (c) RuO_2 (010) on topaz (010), (d) RuO_2 (010) on forsterite (010), and (e) NbO_2 (101) on Mg_2SiO_4 (010).

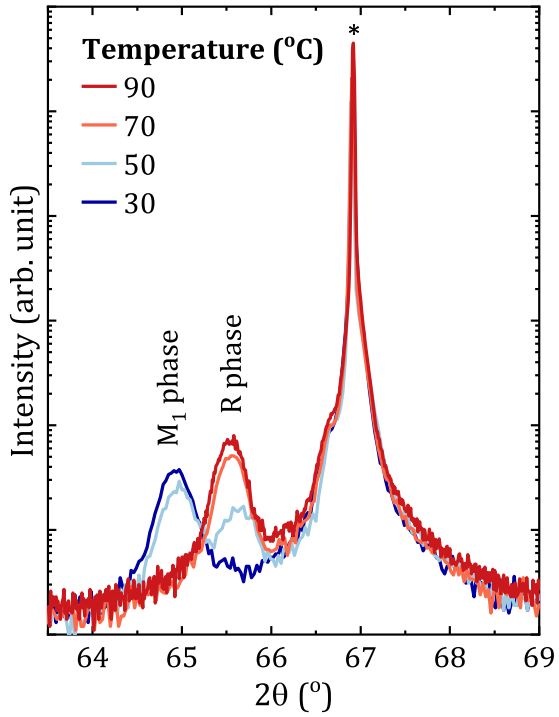

FIG. 28. Variable-temperature XRD of VO_2 on topaz (001) indicating the monoclinic to tetragonal phase transition.

REFERENCES

[1] J. P. Ruf, H. Paik, N. J. Schreiber, H. P. Nair, L. Miao, J. K. Kawasaki, J. N. Nelson, B. D. Faeth, Y. Lee, B. H. Goodge, B. Pamuk, C. J. Fennie, L. F. Kourkoutis, D. G. Schlom, and K. M. Shen, "Strain-stabilized superconductivity," Nat. Commun. **12**, 59 (2021).

[2] N. Wadehra, B. Z. Gregory, S. Zhang, N. Schnitzer, Y. Iguchi, Y. E. Li, B. Pamuk, D. A. Muller, A. Singer, K. M. Shen, and D. G. Schlom, "Strain-induced superconductivity in RuO_2 (100) thin-films," Commun. Mater. **6**, 135 (2025).

[3] L. Šmejkal, J. Sinova, and T. Jungwirth, "Beyond conventional ferromagnetism and antiferromagnetism: A phase with nonrelativistic spin and crystal rotation symmetry," Phys. Rev. X **12**, 031042 (2022).

[4] Z. Feng, X. Zhou, L. Šmejkal, L. Wu, Z. Zhu, H. Guo, R. González-Hernández, X. Wang, H. Yan, P. Qin, X. Zhang, H. Wu, H. Chen, Z. Meng, L. Liu, Z. Xia, J. Sinova, T. Jungwirth, and Z. Liu, "An anomalous Hall effect in altermagnetic ruthenium dioxide," Nat. Electron. **5**, 735–743 (2022).

[5] P. Keßler, L. Garcia-Gassull, A. Suter, T. Prokscha, Z. Salman, D. Khalyavin, P. Manuel, F. Orlandi, I. I. Mazin, R. Valentí, and S. Moser, "Absence of magnetic order in RuO_2: Insights from μSR spectroscopy and neutron diffraction," npj Spintron. **2**, 50 (2024).

[6] J. Liu, J. Zhan, T. Li, J. Liu, S. Cheng, Y. Shi, L. Deng, M. Zhang, C. Li, J. Ding, Q. Jiang, M. Ye, Z. Liu, Z. Jiang, S. Wang, Q. Li, Y. Xie, Y. Wang, S. Qiao, J. Wen, Y. Sun, and D. Shen, "Absence of altermagnetic spin splitting character in rutile oxide RuO_2," Phys. Rev. Lett. **133**, 176401 (2024).

[7] C. A. Occhialini, C. Nelson, A. Bombardi, S. Fan, R. Acevedo-Esteves, R. Comin, D. N. Basov, M. Musashi, M. Kawasaki, M. Uchida, H. You, J. Mitchell, V. Bisogni, C. Mazzoli, and J. Pelliciari, "Structural origin of resonant diffraction in RuO_2," arXiv:2510.13767 (2025).

[8] B. Z. Gregory, N. Wadehra, S. Zhang, Y. Wu, S. Poage, J. Strempfer, A. K. Kundu, A. Rajapitamahuni, E. Vescovo, A. Verma, B. Pamuk, J. Ruf, H. Nair, N. J. Schreiber, K. Ahadi, K. M. Shen, D. G. Schlom, and A. Singer, "Resonant diffraction and photoemission inconsistent with altermagnetism in epitaxial RuO_2 films," arXiv:2510.13781 (2025).

[9] F. J. Morin, "Oxides which show a metal-to-insulator transition at the Néel temperature," Phys. Rev. Lett. **3**, 34–36 (1959).

[10] R. F. Janninck and D. H. Whitmore, "Electrical conductivity and thermoelectric power of niobium dioxide," J. Phys. Chem. Solids **27**, 1183–1187 (1966).

[11] G. Bélanger, J. Destry, G. Perluzzo, and P. M. Raccah, "Electron transport in single crystals of niobium dioxide," Can. J. Phys. **52**, 2272–2280 (1974).

[12] A. Chakraborty, R. G. Hernández, L. Šmejkal, and J. Sinova, "Strain-induced phase transition from antiferromagnet to altermagnet," Phys. Rev. B **109**, 144421 (2024).

[13] A. J. Reese, S. Gelin, M. Maalouf, N. Wadehra, L. Zhang, G. Hautier, D. G. Schlom, I. Dabo, and J. Suntivich, "Tracking water dissociation on RuO_2 (110) using atomic force microscopy and first-principles simulations," J. Am. Chem. Soc. **146**, 32080–32087 (2024).

[14] R. J. Soulen, J. M. Byers, M. S. Osofsky, B. Nadgorny, T. Ambrose, S. F. Cheng, P. R. Broussard, C. T. Tanaka, J. Nowak, J. S. Moodera, A. Barry, and J. M. D. Coey, "Measuring the spin polarization of a metal with a superconducting point contact," Science **282**, 85–88 (1998).

[15] A. Anguelouch, A. Gupta, G. Xiao, G. X. Miao, D. W. Abraham, S. Ingvarsson, Y. Ji, and C. L. Chien, "Properties of epitaxial chromium dioxide films grown by chemical vapor deposition using a liquid precursor," J. Appl. Phys. **91**, 7140–7142 (2002).

[16] Z. Hiroi, "Structural instability of the rutile compounds and its relevance to the metal-insulator transition of VO_2," Prog. Solid State Chem. **43**, 47–69 (2015).

[17] V. J. Fratello, L. A. Boatner, H. A. Dabkowska, A. Dabkowski, T. Siegrist, K. Wei, C. Guguschev, D. Klimm, M. Brützam, D. G. Schlom, and S. Subramanian, "Solid solution perovskite substrate materials with indifferent points," J. Cryst. Growth **634**, 127606 (2024).

[18] J. L. MacManus-Driscoll, M. P. Wells, C. Yun, J. W. Lee, C. B. Eom, and D. G. Schlom, "New approaches for achieving more perfect transition metal oxide thin films," APL Mater. **8**, 040904 (2020).

[19] W. Braun, M. Jäger, G. Laskin, P. Ngabonziza, W. Voesch, P. Wittlich, and J. Mannhart, "*In situ* thermal preparation of oxide surfaces," APL Mater. **8**, 071112 (2020).

[20] F. V. E. Hensling, W. Braun, D. Y. Kim, L. N. Majer, S. Smink, B. D. Faeth, and J. Mannhart, "State of the art, trends, and opportunities for oxide epitaxy," APL Mater. **12**, 040902 (2024).

[21] I. Barin, *Thermochemical Data of Pure Substances*, 3rd ed. (Wiley, 1995), p. 1006, 1014, 1682.

[22] S. Chae, L. A. Pressley, H. Paik, J. Gim, D. Werder, B. H. Goodge, L. F. Kourkoutis, R. Hovden, T. M. McQueen, E. Kioupakis, and J. T. Heron, "Germanium dioxide: A new rutile substrate for epitaxial film growth," J. Vac. Sci. Technol. A **40**, 050401 (2022).

[23] Z. Galazka, R. Blukis, A. Fiedler, S. Bin Anooz, J. Zhang, M. Albrecht, T. Remmele, T. Schulz, D. Klimm, M. Pietsch, A. Kwasniewski, A. Dittmar, S. Ganschow, U. Juda, K. Stolze, M. Suendermann, T. Schroeder, and M. Bickermann, "Bulk single crystals and physical properties of rutile GeO_2 for high-power electronics and deep-ultraviolet optoelectronics," Phys. Status Solidi B **262**, 2400326 (2025).

[24] Z. Galazka, R. Uecker, D. Klimm, K. Irmscher, M. Pietsch, R. Schewski, M. Albrecht, A. Kwasniewski, S. Ganschow, D. Schulz, C. Guguschev, R. Bertram, M. Bickermann, and R. Fornari, "Growth, characterization, and properties of bulk SnO_2 single crystals," Phys. Status Solidi A **211**, 66–73 (2014).

[25] K. M. Adkison, S. L. Shang, B. J. Bocklund, D. Klimm, D. G. Schlom, and Z. K. Liu, "Suitability of binary oxides for molecular-beam epitaxy source materials: A comprehensive thermodynamic analysis," APL Mater. **8**, 081110 (2020).

[26] K. Fukushima, G. H. Takaoka, and I. Yamada, "Epitaxial growth of TiO_2 rutile thin films on sapphire substrates by a reactive ionized cluster beam method," Jpn. J. Appl. Phys. **32**, 3561–3565 (1993).

[27] R. W. Balluffi, A. Brokman, and A. H. King, "CSL/DSC lattice model for general crystal-crystal boundaries and their line defects," Acta Metall. **30**, 1453–1470 (1982).

[28] W. H. Baur and A. A. Khan, "Rutile-type compounds. IV. SiO_2, GeO_2 and a comparison with other rutile-type structures," Acta Crystallogr. Sect. B: Struct. Crystallogr. Cryst. Chem. **27**, 2133–2139 (1971).

[29] G. A. Lager, F. K. Ross, F. J. Rotella, and J. D. Jorgensen, "Neutron powder diffraction of forsterite, Mg_2SiO_4: A comparison with single-crystal investigations," J. Appl. Crystallogr. **14**, 137–139 (1981).
[30] A. Dudka, B. Sevastyanov, and V. Simonov, "Refinement of the atomic structure of alexandrite," Sov. Phys.: Crystallogr. **30**, 277–279 (1985).
[31] G. D. Gatta, F. Nestola, G. D. Bromiley, and A. Loose, "New insight into crystal chemistry of topaz: A multi-methodological study," Am. Mineral. **91**, 1839–1846 (2006).
[32] A. Biswas, C. H. Yang, R. Ramesh, and Y. H. Jeong, "Atomically flat single terminated oxide substrate surfaces," Prog. Surf. Sci. **92**, 117–141 (2017).
[33] C. F. Cline, R. C. Morris, M. Dutoit, and P. J. Harget, "Physical properties of $BeAl_2O_4$ single crystals," J. Mater. Sci. **14**, 941–944 (1979).
[34] B. Finkel, Y. D. Eliezri, A. Waldman, and M. Slatkine, "Pulsed alexandrite laser technology for noninvasive hair removal," J. Clin. Laser Med. Surg. **15**, 225–229 (1997).
[35] R. E. Fitzpatrick and M. P. Goldman, "Tattoo removal using the alexandrite laser," Arch Dermatol. **130**, 1508–1514 (1994).
[36] C. B. Finch and G. W. Clark, "Czochralski growth of single-crystal Mg_2SiO_4 (forsterite)," J. Cryst. Growth **8**, 307–308 (1971).
[37] H. Takei and T. Kobayashi, "Growth and properties of Mg_2SiO_4 single crystals," J. Cryst. Growth **23**, 121–124 (1974).
[38] An equivalent notation can be obtained through permutation in the space group *Pnma*.
[39] S. Somiya, S. Hirano, M. Yoshimura, and H. Shima, *Hydrothermal Synthesis of Topaz Crystals* (Springer, 1989), pp. 153–161.
[40] T. V. Setkova, V. S. Balitsky, A. V. Spivak, A. V. Kuzmin, E. Y. Borovikova, P. S. Kvas, L. V. Balitskaya, A. N. Nekrasov, E. S. Zakharchenko, and D. Y. Pushcharovsky, "Crystal growth, composition, structure, and Raman spectroscopy of novel Ga, Ge-rich topaz," J. Cryst. Growth **637–638**, 127723 (2024).
[41] L. Pauling, "The principles determining the structure of complex ionic crystals," J. Am. Chem. Soc. **51**, 1010–1026 (1929).
[42] D. Andeen and F. F. Lange, "Crystal chemistry of interfaces formed between two different non-metallic, inorganic structures," Int. J. Mater. Res. **98**, 1222–1229 (2007).
[43] In the case of pseudocubic perovskites, a single number line suffices to compare lattice parameters of different materials. In the case of tetragonal rutile thin films and highly orthorhombic substrates, one representation does not suffice and several orientations need to be examined individually.
[44] The (010) orientation is indistinguishable from the (100) orientation in undistorted rutiles, but we chose this notation for a convenient comparison with the orthorhombic substrates.
[45] M. Kawasaki, K. Takahashi, T. Maeda, R. Tsuchiya, M. Shinohara, O. Ishiyama, T. Yonezawa, M. Yoshimoto, and H. Koinuma, "Atomic control of the $SrTiO_3$ crystal surface," Science **266**, 1540–1542 (1994).
[46] G. Koster, B. L. Kropman, G. J. H. M. Rijnders, D. H. A. Blank, and H. Rogalla, "Quasi-ideal strontium titanate crystal surfaces through formation of strontium hydroxide," Appl. Phys. Lett. **73**, 2920–2922 (1998).
[47] T. Ohnishi, K. Takahashi, M. Nakamura, M. Kawasaki, M. Yoshimoto, and H. Koinuma, "A-site layer terminated perovskite substrate: $NdGaO_3$," Appl. Phys. Lett. **74**, 2531–2533 (1999).
[48] J. Chang, Y. S. Park, and S. K. Kim, "Atomically flat single-terminated $SrTiO_3$ (111) surface," Appl. Phys. Lett. **92**, 152910 (2008).
[49] J. H. Ngai, T. C. Schwendemann, A. E. Walker, Y. Segal, F. J. Walker, E. I. Altman, and C. H. Ahn, "Achieving A-site termination on $La_{0.18}Sr_{0.82}Al_{0.59}Ta_{0.41}O_3$ substrates," Adv. Mater. **22**, 2945–2948 (2010).
[50] J. E. Kleibeuker, G. Koster, W. Siemons, D. Dubbink, B. Kuiper, J. L. Blok, C. H. Yang, J. Ravichandran, R. Ramesh, J. E. ten Elshof, D. H. A. Blank, and G. Rijnders, "Atomically defined rare-earth scandate crystal surfaces," Adv. Funct. Mater. **20**, 3490–3496 (2010).
[51] A. Biswas, P. B. Rossen, C. H. Yang, W. Siemons, M. H. Jung, I. K. Yang, R. Ramesh, and Y. H. Jeong, "Universal Ti-rich termination of atomically flat $SrTiO_3$ (001), (110), and (111) surfaces," Appl. Phys. Lett. **98**, 051904 (2011).
[52] J. L. Blok, X. Wan, G. Koster, D. H. A. Blank, and G. Rijnders, "Epitaxial oxide growth on polar (111) surfaces," Appl. Phys. Lett. **99**, 151917 (2011).
[53] J. E. Kleibeuker, B. Kuiper, S. Harkema, D. H. A. Blank, G. Koster, G. Rijnders, P. Tinnemans, E. Vlieg, P. B. Rossen, W. Siemons, G. Portale, J. Ravichandran, J. M. Szepieniec, and R. Ramesh, "Structure of singly terminated polar $DyScO_3$ (110) surfaces," Phys. Rev. B **85**, 165413 (2012).
[54] R. Tomar, N. Wadehra, V. Budhiraja, B. Prakash, and S. Chakraverty, "Realization of single terminated surface of perovskite oxide single crystals and their band profile: $(LaAlO_3)_{0.3}(Sr_2AlTaO_6)_{0.7}$, $SrTiO_3$ and $KTaO_3$ case study," Appl. Surf. Sci. **427**, 861–866 (2018).
[55] Y. Yamamoto, K. Nakajima, T. Ohsawa, Y. Matsumoto, and H. Koinuma, "Preparation of atomically smooth TiO_2 single crystal surfaces and their photochemical property," Jpn. J. Appl. Phys. **44**, L511 (2005).
[56] M. Yoshimoto, T. Maeda, T. Ohnishi, H. Koinuma, O. Ishiyama, M. Shinohara, M. Kubo, R. Miura, and A. Miyamoto, "Atomic-scale formation of ultrasmooth surfaces on sapphire substrates for high-quality thin-film fabrication," Appl. Phys. Lett. **67**, 2615 (1995).
[57] S. Smink, L. N. Majer, H. Boschker, J. Mannhart, and W. Braun, "Long-range atomic order on double-stepped Al_2O_3 (0001) surfaces," Adv. Mater. **36**, 2312899 (2024).
[58] M. Brucker, V. Harbola, J. Mannhart, S. Smink, T. J. Whittles, and F. V. E. Hensling, "Morphology of various single faced sapphire surfaces prepared by rapid thermal annealing," Appl. Surf. Sci. **696**, 162929 (2025).
[59] H. Ohta, H. Tanji, M. Orita, H. Hosono, and H. Kawazoe, "Heteroepitaxial growth of zinc oxide single crystal thin films on (111) plane YSZ by pulsed laser deposition," MRS Proc. **570**, 309 (1999).
[60] T. Nakamura, Y. Tokumoto, R. Katayama, T. Yamamoto, and K. Onabe, "RF-MBE growth and structural characterization of cubic InN films on yttria-stabilized zirconia (001) substrates," J. Cryst. Growth **301–302**, 508–512 (2007).
[61] We switched to a tube furnace to avoid long annealing times inside the MBE growth chamber. There is no fundamental reason that prohibits long-duration *in situ* annealing processes. A key difference, however, is the attainable gas pressure. While pressures higher than 1×10^{-5} Torr are difficult to achieve in our vacuum tools, 1 atm oxygen pressure can readily be obtained in a tube furnace. The main advantage of *ex situ* tube furnace annealing is the ability to prepare many sample simultaneously in parallel.
[62] $BeAl_2O_4$ is insoluble in all acids, preventing us from exploring chemical treatment alternatives to the high-temperature annealing.
[63] M. S. Hampar and J. Zussman, "The thermal breakdown of topaz," TMPM, Tschermaks Mineral. Petrogr. Mitt. **33**, 235–252 (1984).
[64] M. S. Hampar and J. Zussman, "Damage of topaz and other minerals in the electron microscope," TMPM, Tschermaks Mineral. Petrogr. Mitt. **31**, 27–37 (1983).
[65] J. W. Tashman, J. H. Lee, H. Paik, J. A. Moyer, R. Misra, J. A. Mundy, T. Spila, T. A. Merz, J. Schubert, D. A. Muller, P. Schiffer, and D. G. Schlom, "Epitaxial growth of VO_2 by periodic annealing," Appl. Phys. Lett. **104**, 063104 (2014).
[66] H. Paik, J. A. Moyer, T. Spila, J. W. Tashman, J. A. Mundy, E. Freeman, N. Shukla, J. M. Lapano, R. Engel-Herbert, W. Zander, J. Schubert, D. A. Muller, S. Datta, P. Schiffer, and D. G. Schlom, "Transport properties of ultra-thin VO_2 films on (001) TiO_2 grown by reactive molecular-beam epitaxy," Appl. Phys. Lett. **107**, 163101 (2015).
[67] S. Hazra, T. Schwaigert, A. Ross, H. Lu, U. Saha, V. Trinquet, B. Akkopru-Akgun, B. Z. Gregory, A. Mangu, S. Sarker, T. Kuznetsova, S. Sarker, X. Li, M. R. Barone, X. Xu, J. W. Freeland, R. Engel-Herbert, A. M. Lindenberg, A. Singer, S. Trolier-McKinstry, D. A. Muller, G. M. Rignanese, S. Salmani-Rezaie, V. A. Stoica, A. Gruverman, L. Q. Chen, D. G. Schlom, and V. Gopalan, "Colossal strain tuning of ferroelectric transitions in $KNbO_3$ thin films," Adv. Mater. **36**, 2408664 (2024).